ACS APPLIED OPTICAL MATERIALS

pubs.acs.org/acsaom Article

Nanoscale Characterization of Individual Three-Dimensional Split Ring Resonator Systems

C. Praise Anyanwu,[‖] Grace Pakeltis,[‖] Philip D. Rack,* and David J. Masiello*

Cite This: ACS Appl. Opt. Mater. 2023, 1, 607−614 Read Online

ACCESS | Metrics & More | Article Recommendations

ABSTRACT: In this work, we investigate the hybridization of three-dimensional plasmonic split ring resonator (SRR) pairs using focused electron beam nanospectroscopy and model their combined electric and magnetic responses using electromagnetic theory and numerical calculations. Specifically, we fabricate three-dimensional (3D) SRR dimers with varying in-plane rotations and out-of-plane tilts and perform electron energy loss spectroscopy (EELS) measurements to elucidate the impact of their 3D electric and magnetic interactions on the EEL spectrum of each individual SRR dimer. On the basis of the competition between the SRR's electric and magnetic interactions within our model, we find that varying the 3D tilt angle diminishes the magnetic coupling but increases the level of overall mode mixing. Through further modeling of the experimental data, we determine the system's electric and magnetic coupling constants, as well as the overall effective coupling constant, a useful metric for characterizing the strength of light−matter interaction. We additionally explore the potential for geometric frustration in the magnetic mode ordering of a coupled SRR trimer using both EELS experiment and companion theoretical modeling. Taken together, the insight gained into the behavior of coupled 3D SRRs serves as a stepping stone to the rational design of 3D photonic metamaterials endowed with even richer optical functionality.

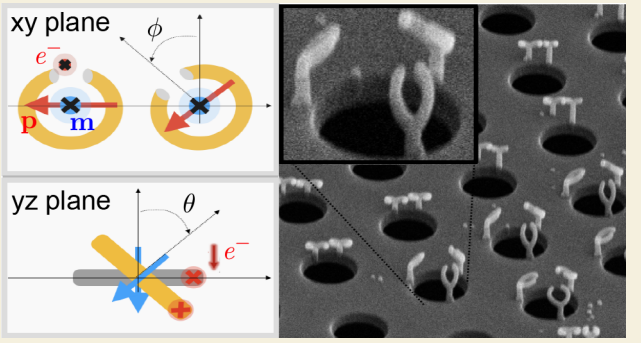

KEYWORDS: *electron energy loss spectroscopy (EELS), scanning transmission electron microscopy (STEM), split ring resonators (SRR), plasmon hybridization, focused electron beam-induced deposition (FEBID)*

INTRODUCTION

Negative index of refraction (NIR) metamaterials have become significantly important in nanophotonics owing to their remarkable optical properties that cannot be achieved in naturally occurring materials.[1−8] Fundamental to the design of NIR metamaterials is the split ring resonator (SRR), which has been used in a variety of applications, including perfect lenses,[9−12] biosensors,[13,14] antennas,[15,16] and absorbers and filters.[17,18] When arranged in an array, individual SRRs act as "atoms" with the emergent optical properties of the metamaterial arising through their mutual coupling, thus providing an impetus for detailed studies of the fundamental two-body interactions between pairs of SRR units.[19,20]

While far-field optical characterization techniques are commonly used to investigate SRR-based metamaterials,[21,22] few studies have employed subdiffraction-limited probes such as scanning transmission electron microscopy (STEM) electron energy loss spectroscopy (EELS) to measure SRR couplings at their own native length scale.[23] STEM-EELS provides nanometer-scale spatial information together with correlated spectroscopic responses capable, e.g., of revealing dark modes that cannot be detected by far-field characterization tools. Clear distinction of the bright and dark modes is critical to quantify the strength and to elucidate the nature of light−matter interaction. In ref 24, von Cube et al. showed the progression from distinct optically bright and dark eigenmodes in small arrays (i.e., two to four SRRs) to the formation of a quasi-continuum of modes in the interior, and edge modes at the boundaries of a large array. In another EELS study, Liang et al.[25] investigated individual Au SRR dimers, fabricated with 0°, 90°, and 180° relative planar angles to elucidate the hybridization of their fundamental modes. These studies combined numerical simulations with experimental EELS measurements to elucidate the interplay between the SRR's electric and magnetic dipole moments in the hybridization of coupled SRRs within a planar or two-dimensional geometry.

Received: November 10, 2022
Accepted: January 3, 2023
Published: January 25, 2023

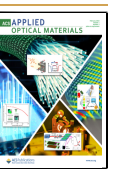

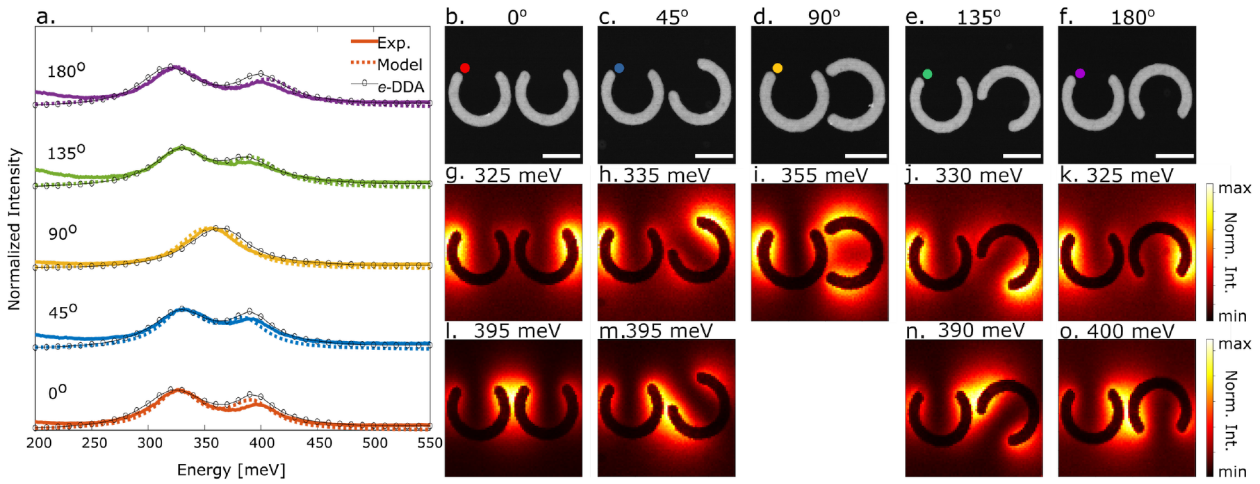

Figure 1. (a) Experimental (solid), theoretical model (dashed), and numerical *e*-DDA simulation (circle) EEL spectra taken at the SRR outer tip for the planar rotational study. (b–f) HAADF images of each SRR dimer with a colored circle indicating where the spectra in panel a were acquired. Corresponding spectrum images show the (g–k) lower-energy and (l–o) higher-energy normal modes of the system. The scale bar is 300 nm.

Beyond planar structures, little consideration has been given to three-dimensional (3D) SRRs with electric and magnetic responses that can be oriented arbitrarily in 3D space, which would produce an even richer set of interactions and emergent responses. Bicket et al.[26] investigated "vertically" oriented SRRs using cathodoluminescene and EELS to study the fundamental magnetic dipole mode. However, due to challenges in fabricating 3D SRRs, it remains difficult to clearly distinguish the magnetic mode and elucidate its role in the hybridization of SRR pairs. To this end, the work presented in ref 27 achieves a breakthrough in fabricating plasmonic 3D SRR nanoresonators, using focused electron beam-induced deposition (FEBID) to deposit nonplasmonic 3D scaffolds, which are subsequently isolated with a conformal SiO_2 layer and then coated with a gold layer to create functional 3D plasmonic nanostructures. Building from this work, here we investigate the effect of 3D out-of-plane tilting on the electric and magnetic dipole couplings in individual nanofabricated SRR dimers, and the downstream impacts in metamaterial design using monochromated aberration-corrected STEM-EELS and companion theoretical modeling.

The STEM-EELS measurements presented in this study expose the effects of 3D geometry upon the interaction between individual SRRs. Theoretical analysis of the observed data accounts for the induced electric and magnetic dipoles on each SRR as well as their mutual near-field couplings in SRR dimers as probed by STEM electron beam. We then map the dynamics of the SRR surface current density onto effective oscillator equations of motion, with an effective coupling constant exhibiting both two-dimensional (2D) and 3D angular dependence. This description is well suited for an analytic analysis of the EEL probability, which shows that for a particular orientation, increasing the 3D tilt angle diminishes the magnetic coupling but enhances the overall light–matter interaction strength. On the basis of this model, we additionally examine the hybridization of individual 2D SRR trimers measured using EELS. Taken together, this study elucidates the geometric effects of 3D tilt on the SRR magnetic dipole moment and its role in the hybridization of coupled 3D SRRs, thus serving as a stepping stone for nanoengineering NIR metamaterials composed of coupled 3D SRR units.

RESULTS AND DISCUSSION

Figures 1 and 2 display a series of Au SRR pairs with varying in-plane orientations and out-of-plane tilts, each SRR with a 450 nm diameter and a 270° arc length. To provide a baseline for the out-of-plane tilting in the 3D study, first, a pair of SRRs are lithographically patterned on a SiN_x membrane, with a relative planar angle of 0°, 45°, 90°, 135°, or 180°, as shown in the top panel (Figure 1b–f). Experimental EELS measurements are performed on each SRR pair, with the electron beam probe positioned at the colored dots, traveling into the plane of the page. Figure 1a displays the corresponding color-coded EEL spectra showing a single peak for the 90° orientation and a clear peak splitting into bonding and antibonding dipolar modes for the 0°, 45°, 135°, and 180° planar orientations. The signatures of the bonding and antibonding modes are identified by the experimental EEL spectrum images, illustrated in Figure 1g–o. The in-phase bonding modes are observed in the lower-energy maps (Figure 1g,h,j,k) with the zero EELS intensity signature in the gap, while the out-of-phase antibonding modes are observed in the higher-energy maps (Figure 1l–o) with the high-EELS intensity signature in the gap.

The geometric effect on the spectrum of a coupled pair of SRRs, arbitrarily oriented in space, results from their doubly coupled electromagnetic interaction. In particular, the progression of the mode mixing in the STEM-EELS of Figure 1 is a known characteristic behavior that stems from the interplay between electric and magnetic interactions of coupled planar SRRs.[19,28] Describing the EEL spectra within a model that can be generalized to three dimensions requires knowledge of the potential energy of interaction between the SRR and the evanescent electric field of a STEM electron beam, as well as the interaction energy between coupled SRRs.

Analysis of the Electron Beam-Driven SRR Dimer

An electron beam oriented to point into the plane of the page of Figure 1 drives current about the circular path of one of the pair of SRRs, with the following interaction potential energy

https://doi.org/10.1021/acsaom.2c00157
ACS Appl. Opt. Mater. 2023, 1, 607–614

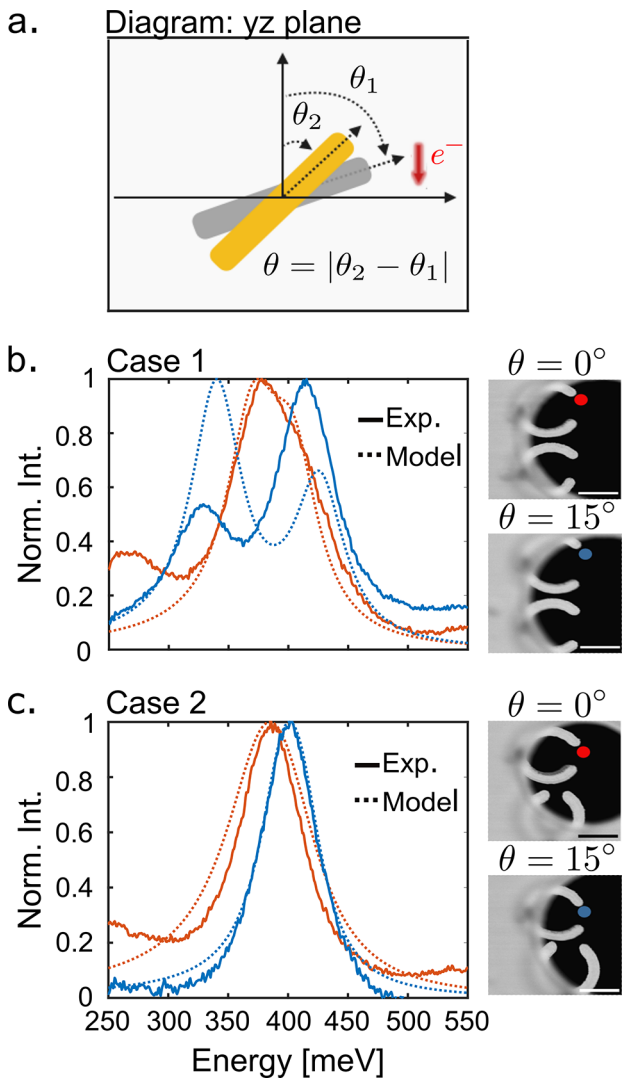

Figure 2. EEL spectra of individual, coupled, and 3D SRR dimers. For each dimer, the SRRs are placed side by side. (a) Diagram depicting the side view of the SRR dimer and the 3D tilt angles (θ_1 and θ_2) of the first and second SRRs. The relative 3D tilt angle between the two SRRs is $\theta = |\theta_2 - \theta_1|$, which attenuates the magnetic dipole interaction in eq 12. (b) Experimental (solid) and model (dashed) EEL spectra, with the electron probe placed at the outer tip of the first SRR. For each tilt study, the point EEL spectrum is color-coded with respect to a color-coded dot (representing the electron probe) on the adjacent HAADF image that shows a top-down view of the SRR dimer. For the red curves, the 3D out-of-plane tilt angles (θ_1, θ_2) = (30°, 30°), respectively, for the electron probe-driven and undriven SRRs in the dimer, while for the blue curves, (θ_1, θ_2) = (30°, 45°), respectively. (c) Planar orientation for the SRR dimer as shown in Figure 1d and EEL spectra acquired for same the 3D tilt orientations conducted in panel b.

$$U_{el} = \oint_{\partial \mathbf{x}_1} \mathbf{F}_{el} \cdot d\mathbf{x}_1 \approx q_1 \mathbf{E}_{el} \cdot \mathbf{x}_1 \quad (1)$$

where q_1 is the total charge for the fundamental dipole mode. Thus, the force from the electron beam polarizes the driven SRR in the direction defined by the unit vector $\hat{\mathbf{x}}_1 = \mathbf{x}_1/s$ across the split of the ring of width s. The polarized field induced on the SRR has a dominant dipolar electromagnetic response that prevails within the spectral window of the STEM-EELS analysis, and it is well separated from higher-energy modes.[27] With its large distance to the second SRR, the influence of the electron beam upon the second SRR is neglected, with the beam positioned at each of the bullets in the top panels of Figure 1b–f.

The induced current about the circular path of the driven SRR sets up a magnetic dipole moment whose field is normal to the SRR plane and orthogonal to the electric dipole field set across the split direction. It is through this electric field and induced magnetic flux density of these electric and induced magnetic dipoles that the two SRRs interact. The interaction can be expressed from the Lorentz force, such that

$$U_{12} = \oint_{\partial \mathbf{x}_2} \mathbf{F}_1 \cdot d\mathbf{x}_2 = q_2 \oint_{\partial \mathbf{x}_2} \left(\mathbf{E}_1 + \frac{\mathbf{v}_2}{c} \times \mathbf{B}_1 \right) \cdot d\mathbf{x}_2 \quad (2)$$

where $\mathbf{E}_1$ and $\mathbf{B}_1$ are the electric field and the induced magnetic flux density, respectively, both from the first ring, acting on the closed circular, surface path $\partial \mathbf{x}_2$ of the second ring. In this system, drift velocity $\mathbf{v}_2$ about the second ring is due to the current induced by field $\mathbf{E}_1$. To clarify the interaction mechanism, we express the interaction potential as

$$\begin{aligned} U_{12} &= q_2 \oint_{\partial \mathbf{x}_2} \mathbf{E}_1 \cdot d\mathbf{x}_2 + q_2 \oint_{\partial \mathbf{x}_2} \left(\frac{\mathbf{v}_2}{c} \times \mathbf{B}_1 \right) \cdot d\mathbf{x}_2 \\ &= q_2 \oint_{\partial \mathbf{x}_2} \mathbf{E}_1 \cdot d\mathbf{x}_2 - q_2 \oint_{\partial \mathbf{x}_2} \mathbf{B}_1 \cdot \left(\frac{\mathbf{v}_2}{c} \times d\mathbf{x}_2 \right) \\ &\approx \mathbf{E}_1 \cdot \mathbf{p}_2 - \mathbf{B}_1 \cdot \mathbf{m}_2 \end{aligned} \quad (3)$$

where $\mathbf{p}_2 = q_2 \mathbf{x}_2$ and $\mathbf{m}_2 = q_2(\mathbf{v}_2/c) \times \mathbf{x}_2$ are the induced electric and magnetic dipole moments of the second SRR, respectively, with $\mathbf{p}_2$ pointing in direction $\hat{\mathbf{x}}_2$ across the split and $\mathbf{m}_2$ pointing in the direction $\hat{\mathbf{v}}_2 \times \hat{\mathbf{x}}_2$ normal to the SRR plane. For the orientation in Figure 1d, $\mathbf{E}_1$ and $\mathbf{p}_2$ are orthogonal so the first term vanishes and the interaction is purely magnetic, however small, resulting in a weak mode mixing and thus a negligible spectral splitting of the normal modes. However, in panels a and b of Figure 1, $\mathbf{E}_1$ and $\mathbf{p}_2$ are either in phase or out of phase, resulting in a deconstructive or constructive interaction with the magnetic field, thus giving rise to mode mixing having varying normal mode splitting.

Theoretical Description of the EEL Spectra

The following paragraphs describe the derivation of an analytic expression for the observed STEM-EELS measurements in Figures 1 and 2. EELS measurements are capable of resolving the in-plane ϕ and out-of-plane θ angular dependence of the interaction terms defined in eq 3. These interaction terms relate to the coupling constant quantifying the strength of light–matter interaction between the coupled SRR pair. This coupling constant will quantify the geometric effect of 3D tilting on mode mixing in Figure 2.

Figure 2 shows a 3D tilt study of coupled SRR dimers placed side by side. The setup is shown in Figure 2a, depicting a side view of the SRRs and their 3D tilt angles, and in Figure 2b, the adjacent high-angle annular dark-field (HAADF) image shows a top-down view of the SRRs. The top SRR tilts out of plane at $\theta_1 = 30°$, and the bottom SRR tilts at $\theta_2 = 30°$ (top panel) and $\theta_2 = 45°$ (bottom panel). Thus, for the top and bottom panels,

https://doi.org/10.1021/acsaom.2c00157
ACS Appl. Opt. Mater. 2023, 1, 607–614

the relative tilt angles between the top and bottom SRRs are $\theta = 0°$ and $\theta = 15°$, respectively (as depicted in Figure 2a). The EEL spectra in panels b and c are measured with the electron beam placed at the colored circles at the outer tip of the top SRR. In both spectra, the hybridized modes result from the electric and induced magnetic dipole interactions.

In contrast, Figure 2c shows a case in which the bottom SRR has been rotated 90° in plane to uncouple the electric-field interaction between both SRRs. The result is a weakly coupled dimer, as shown in the negligible spectral splitting, due to a weak, purely magnetic interaction, and as the bottom SRR tilts out of plane at 45°, the magnetic interaction weakens further and the spectrum reduces to the uncoupled system identical to the SRR monomer.

To evaluate the electric and magnetic coupling constants and to analyze the role of the magnetic interaction in the STEM-EEL measurements of Figures 1 and 2, we will need to derive the EEL probability per unit frequency[29,30]

$$\Gamma_{\mathrm{EEL}}(\omega) = \frac{|\mathbf{E}_{\mathrm{el}}(\mathbf{R}, \omega)\cdot\hat{\mathbf{x}}_1|^2}{\pi\hbar}\,\mathrm{Im}\,\alpha_1(\omega) \tag{4}$$

of an SRR dimer from a model containing both electric and magnetic interactions. In this expression, $\mathbf{E}_{\mathrm{el}}(\mathbf{R})$ is the evanescent field of the STEM electron probe located at impact parameter $\mathbf{R}$ and α_1 is the polarizability of the first SRR coupled to the second SRR via near-field electric and magnetic dipole interactions. Together, these quantities define induced dipole moment $\mathbf{p}_1$

$$\alpha_1(\omega)\mathbf{E}_{\mathrm{el}}(\mathbf{R}, \omega) = q_1(\omega)\mathbf{x}_1 \tag{5}$$

expressed in terms of dynamical coordinate $q_1(\omega)$ representing the total charge on the driven SRR. The Lagrangian governing the dynamics of the coupled SRR dimer in the external field of the electron beam is given by

$$\begin{aligned} L &= T - U_{12} - U_{\mathrm{el}} \\ &= \sum_i A\dot{q}_i^{\,2} - \sum_i B q_i^{\,2} - \frac{1}{2}\sum_{\substack{ij \\ i\neq j}} [\mathbf{E}_i(q_i)\cdot\mathbf{p}_j - \mathbf{B}_i(\dot{q}_i)\cdot\mathbf{m}_j] \\ &\quad - \sum_i \mathbf{E}_{\mathrm{el}}\cdot\mathbf{p}_i \end{aligned} \tag{6}$$

with $i, j = 1, 2$. The generalized coordinate is the time-dependent amplitude of total charge $q_i(t)$ on each SRR. More so, assuming identical SRRs, A and B are constants equal across both SRRs. The quantity A has dimensions of inductance (square seconds per centimeter), which behaves as the inertial quantity analogous to the mass on a mechanical oscillator. It follows that B has units of inverse capacitance (inverse centimeters), such that the resonance frequency of the SRR is given by $\sqrt{B/A}$. Then the simplified Lagrangian yields

$$L = A[\sum_i \dot{q}_i^{\,2} - {\omega_0}^2 q_i^{\,2} + \frac{1}{2}\sum_{\substack{ij \\ i\neq j}} (\beta\dot{q}_i\dot{q}_j - g_{\mathrm{E}} q_i q_j)] - \sum_i (\mathbf{E}_{\mathrm{el}}\cdot\mathbf{x}_i) q_i \tag{7}$$

where β and g_{E} are geometric coupling constants of the near-field electric and magnetic interactions, respectively. In the absence of the drive field of the electron beam, eq 7 is similar to the well know Lagrangian of coupled SRRs.[20,31−34] However, eq 7 yields steady state solution $q_1(\omega)$ of the electron beam-driven, coupled SRR.

It follows that the Euler−Lagrange equations of motion produce an electric, position-dependent coupling, as well as a magnetic, velocity-dependent coupling. Following the procedure outlined in ref 35 (Appendix A), a linear transformation of the Euler−Lagrange equations from eq 7 yields the following coupled effective oscillator equations of motion representing the coupled fundamental dipolar modes of an SRR pair, such that

$$\ddot{q}_1(t) + \gamma_0\dot{q}_1 + {\Omega_0}^2 q_1 + G q_2 = -\frac{\mathbf{E}_{\mathrm{el}}\cdot\mathbf{x}_1}{2A} \tag{8}$$

$$\ddot{q}_2(t) + \gamma_0\dot{q}_2 + {\Omega_0}^2 q_2 + G q_1 = 0 \tag{9}$$

where in an ad hoc fashion we have added a term that depends on the generalized velocity for dissipative loss of rate $\gamma_0=\gamma_1 = \gamma_2$. Note that the dimer system bears new effective oscillator parameters, with defined effective resonance frequency and coupling constant, i.e.

$${\Omega_0}^2 = {\omega_0}^2 - \frac{g_{\mathrm{E}}\beta}{4} \tag{10}$$

$$G_{\mathrm{eff}} = \frac{|G|}{\Omega_0} \tag{11}$$

Coupling constant G expresses the angular dependence of the electric and magnetic near-field interaction such that

$$\begin{aligned} G &= [g_{\mathrm{E}}(\phi) - \beta(\theta){\omega_0}^2]/2 \\ &= [g_{\mathrm{E}}(\phi) - g_{\mathrm{B}}(\theta)]/2 \\ &= [g_{\mathrm{E}}\cos\phi - g_{\mathrm{B}}\cos\theta]/2 \end{aligned} \tag{12}$$

where angles ϕ and θ correspond to the relative in-plane rotation and out-of-plane tilts, respectively, of the second SRR with respect to the first, as shown in Figures 1 and 2. Finally, we express the dynamics of the total charge on the driven SRR dipole oscillator in the frequency domain as

$$q_1(\omega) = \frac{-\mathbf{E}_{\mathrm{el}}(\mathbf{R}, \omega)\cdot\mathbf{x}_1}{2A}\,\frac{1}{{\Omega_0}^2 - \omega^2 - i\gamma_1\omega - \frac{G^2}{{\Omega_0}^2 - \omega^2 - i\gamma_2\omega}} \tag{13}$$

Equation 13 yields the solution to eq 5, the polarizability of the driven SRR. The self-energy term in the denominator of eq 13 expresses the perturbation due to the near-field interaction with the second SRR. With these equations, the analytic expression of the EEL probability distribution function in eq 4 and the effective coupling constant in eqs 11 and 12 capture the behavior of the observed STEM-EELS measurements in Figures 1 and 2.

To illustrate, first, in Figure 1 (without tilting, $\theta = 0°$), the strength of the light−matter interaction ($G_{\mathrm{eff}} = |G|/\Omega_0$) approaches a minimum and maximum value for the planar orientations $\phi = 90°$ and $\phi = 180°$, respectively. The latter value corresponds to the normal mode spectral splitting of the coupled SRR pair. For instance, the weak interaction strength at $\phi = 90°$ is due to the purely magnetic interaction $G = [g_{\mathrm{E}}\sin(\phi = 90) - g_{\mathrm{B}}\cos(\theta = 0)]/\Omega_0 = -g_{\mathrm{B}}/\Omega_0$. More so, eq 12 predicts that 3D tilting ($\theta \neq 0$) has the effect of strengthening SRR couplings by decreasing the counteraction of the induced magnetic interaction on the strong electric interaction. As in Figure 2b, the spectral splitting increases as the 3D tilt angle

https://doi.org/10.1021/acsaom.2c00157
ACS Appl. Opt. Mater. 2023, 1, 607−614

increases. This result justifies the claim that tilting out of plane diminishes the induced magnetic interaction, yet enhancing the overall light−matter interaction between coupled SRRs. These trends are further supported via numerical electromagnetic simulations of the coupled SRR system using the electron beam-driven discrete dipole approximation (*e*-DDA).

Furthermore, Figure 2c explores the purely induced magnetic interaction in 3D. First, the initial frame of the SRR pair is as such in the orientation at $\phi = 90°$. Then the undriven, coupled SRR is tilted out of plane. In this case, the coupling strength decreases to the simple expression $G = -(g_B/\Omega_0)\cos\theta$. Thus, tilting out of plane (where $\theta \to 90°$) results in a negligible near-field interaction, and the spectra reduce to the case of the uncoupled system identical to the SRR monomer, as observed in Figure 2c and in the estimates of the fit parameters in Table 1. In general, this 3D tilt study distinguishes the magnetic dipole and characterizes its role in the hybridization scheme of coupled SRRs.

Table 1. 3D Parameter Estimates

ϕ (deg)	θ (deg)	$\hbar\Omega_0$ (meV)	$\hbar\gamma_0$ (meV)	$\hbar G_{eff}$ (meV)	$\hbar\omega_0$ (meV)
0	0	389	52	33	410
0	15	387	51	85	410
90	0	390	78	20	410
90	15	404	48	15	410

Model Application: Estimating the Interaction Strength of Coupled SRRs

As mentioned, Figure 1 provides a baseline for the 3D study. Applying the EEL probability distribution function in eq 4 as a fit function to the data in Figure 1 yields estimates for the system parameters (see Table 2). First, the fit of eq 4 to the numerical *e*-DDA simulation data of the SRR monomer spectrum (parametrized according to the idealized experimental SRR system parameters in the absence of the supporting substrate) yields estimates of natural resonance frequency ω_0 and inductance A. Then the fit to the simulation data of the SRR dimer spectrum at the initial orientation (Figure 1b; $\phi = 0°$) and the pure magnetic orientation (Figure 1d; $\phi = 90°$) yields estimates of coupling constant magnitudes g_E and g_B. With these parameters, calculations using eqs 10 and 12 yield effective resonance frequency Ω_0 and coupling constant G. The values of Ω_0 and G calculated from the model serve as bounds for the fitting procedure to the experimental STEM-EELS measurements, from which the true values of Ω_0 and G are determined. We note that in the fitting procedure outlined, γ_0 is the only free parameter. Finally with the estimates of the system parameters, as shown in Table 2, the model is overlaid on the STEM-EEL spectra.

Table 2. Parameter Estimates

A(s^2 cm^{-1})	$\hbar\omega_0$ (meV)	$\hbar^2 g_E$ (meV^2)	$\hbar^2 g_B$ (meV^2)
1.885×10^{-31}	359	6.5×10^{-2}	9.0×10^{-3}
ϕ (deg)	$\hbar\Omega_0$ (meV)	$\hbar\gamma_0$ (meV)	$\hbar G_{eff}$ (meV)
0	362	47	65
45	360	47	54
90	359	47	25
135	365	55	64
180	370	58	82

Applying parameter estimates A, ω_0, g_E, and g_B to eqs 10 and 12 for Ω_0 and G yields the normal mode energies $\hbar\Omega_{\mp} = \hbar\sqrt{\Omega_0(\phi,\theta)^2 \mp G(\phi,\theta)}$. Figure 3a is the anticrossing graph of the normal mode energies. These normal mode calculations are benchmarked with the fit estimates of Ω_0 and G from numerical *e*-DDA simulations and the experimental data. In essence, Figure 3a shows that changing the orientation of the SRRs tunes the degree of normal mode mixing, where Ω_- and Ω_+ are the in- and out-of-phase normal mode energies whose mode profiles are shown in the electromagnetic-field maps of Figure 3b−s.

Moreover, the electromagnetic-field maps in Figure 3b−s show a phase change in the normal mode of the induced magnetic dipoles when the second coupled SRR changes orientation from $\phi = 0°$ to $\phi = 180°$. For example, the magnetic fields of the induced magnetic dipoles are in phase in the lower-energy normal mode at $\phi = 0°$ but out of phase at $\phi = 180°$ (see Figure 3g,k). This apparent inversion is due to Faraday's law of induction; i.e., changing the orientation of the coupled SRR from $\phi = 0°$ to $\phi = 180°$ changes the direction of the induced current about its loop and, thus, changes the direction of the magnetic field normal to its plane.

Magnetic Ordering of the SRR Trimer

In Figure 4, a planar trimer of SRRs (450 nm diameter, 270° arc length) is arranged in a D_{3h} symmetry to explore the effects of geometric frustration in the magnetic dipole ordering of its normal modes. EEL spectra are acquired at the inner arm and at the gap of the SRR trimer (see colored dots in the HAADF image in Figure 4a) to preferentially excite the lower- and higher-energy normal modes, respectively. Note that the beam position located in the gap center (blue) excludes the lower-energy in-phase normal mode by symmetry. Figure 4b shows the measured EEL spectra (normalized to the zero loss peak) with resonant energies at 300 and 400 meV, while panels c and d of Figure 4 display the measured spectrum images collected at these resonant energies. The results from numerical EEL simulation of the SRR trimer (Figure 4e−i) show the electric and magnetic mode profiles of the in-phase lower-energy normal mode (Figure 4e,g) and out-of-phase higher-energy normal mode (Figure 4f,h), which is doubly degenerate. These field profiles are consistent with their respective measured spectrum images from panel c.

In the lower-energy normal mode, the electric dipoles are in phase (all pointing head to tail), and in this point group symmetry, the direction of the circular current is the same on each loop of the SRR. This gives rise to magnetic dipole moments with ferromagnetic (FM) ordering (all pointing out of plane). In the higher-energy normal mode, however, the electric dipoles are out of phase, and thus, the direction of the circular current is different on each loop of the SRR. This gives rise to a pair of doubly degenerate magnetic dipole moments with antiferromagnetic (AFM) ordering. Thus, by correlating experimental EELS measurements with calculated induced electric- and magnetic-field profiles, Figure 4 shows that the magnetic dipole ordering within a given SRR trimer normal mode is dictated by the specific current path about each loop of each SRR as excited by the STEM electron probe at particular impact parameters.

CONCLUSION

In this paper, we combine a STEM-EELS experiment with theoretical modeling to study the 3D geometric effects of

https://doi.org/10.1021/acsaom.2c00157
ACS Appl. Opt. Mater. 2023, 1, 607−614

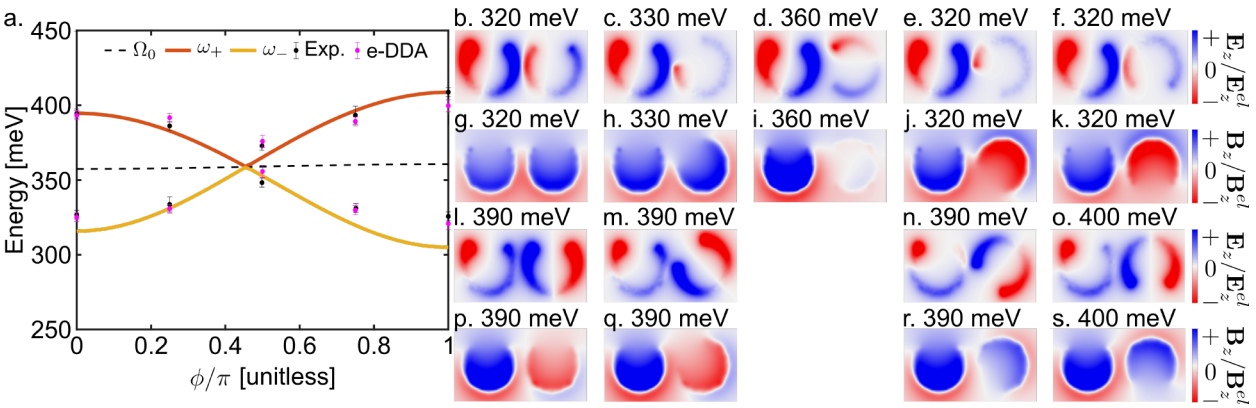

Figure 3. (a) Anticrossing of the normal mode energies from the derived analytical expression $\hbar\Omega_{\mp} = \hbar\sqrt{\Omega_0(\phi, \theta)^2 \mp G(\phi, \theta)}$ (solid) and fit estimates of the experimental (black dots) and numerical *e*-DDA (magenta dots) normal mode energies for the planar rotational study in Figure 1. The progression of the normal mode splitting is tuned by changing the coupling strength as a function of the in-plane ϕ orientation of the second SRR. Numerical *e*-DDA electric-field (b–f) and magnetic-field (g–k) profiles of the bonding modes are compared against electric-field (i–o) and magnetic-field (p–s) profiles of the antibonding modes.

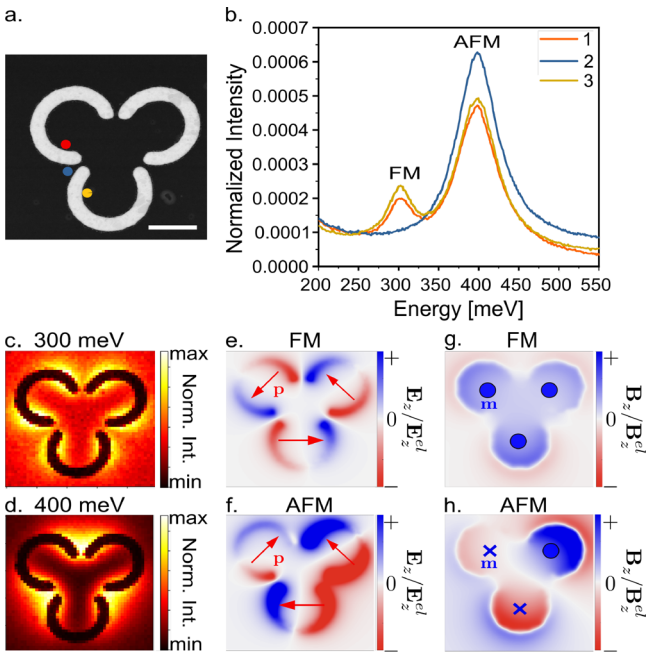

Figure 4. EEL point spectra, spectrum images, and induced electric- and magnetic-field profiles of a planar SRR trimer with D_{3h} symmetry. (a) HAADF image of the trimer. The scale bar is 300 nm. (b) Experimental EEL spectra acquired at the beam positions indicated in panel a. (c and d) Experimental spectrum images at the resonant energies of 300 and 400 meV with FM and AFM ordering, respectively, shown in the simulated field profiles of (e) the electric dipole in-phase lower-energy normal mode, (f) the electric dipole out-of-phase higher-energy normal mode, (g) the magnetic dipole in-phase lower-energy normal mode, and (h) the magnetic dipole out-of-phase higher-energy normal mode.

electric and magnetic plasmon mode mixing in nanofabricated 3D SRR dimers with varying out-of-plane tilt angles. Spectral splitting of the normal modes arising from the 3D tilt has been interpreted by theoretically mapping the SRR electromagnetic responses onto effective dipole oscillators, with an effective coupling that reveals a competition between interactions mediated by electric and magnetic SRR dipole fields. Importantly, our results confirm that varying the 3D tilt angle between coupled SRRs diminishes the magnetic coupling but enhances the overall mode mixing, and for a certain planar orientation and tilt angle, the SRR dimer becomes uncoupled, with a response reminiscent of a single SRR. We have also described the influence of the electric dipole's circular current path on the magnetic ordering of a coupled SRR trimer arranged in a planar triangular D_{3h} symmetry, where the hybridized magnetic dipoles are ferromagnetically ordered in the lower-energy in-phase normal mode and antiferromagnetically ordered in the higher-energy out-of-phase normal mode. The EELS measurements and corresponding theoretical analysis presented in this study shed light on the rational design of a new class of NIR metamaterials formed from embedded 3D SRR units.

MATERIALS AND METHODS

Planar SRR Fabrication

The planar split ring resonators are fabricated via electron beam lithography (JEOL 9300FS) using a lift-off process. A 300 μm Si wafer with 30 nm of low-pressure chemical vapor-deposited SiN_x is spin coated with PMMA 495 A4 and exposed. The pattern is then developed using a 1:3 methyl isobutyl ketone/isopropyl alcohol (IPA) mixture. Twenty-five nanometers of Au is sputter deposited via dc magnetron sputtering onto the substrate followed by soaking in a heated NMP bath, sonicating in NMP and acetone, and rinsing with IPA and deionized water. The backside of the wafer is then spin coated with P20 and S1818 and exposed using photolithography to create the windows of the transmission electron microscope. Reactive ion etching is used to remove the backside nitride layer, and the wafer is subsequently submerged in a heated KOH bath to etch the Si windows and TEM grid edges.

3D SRR Fabrication

3D split ring resonators were fabricated using a hybrid synthesis approach utilizing focused electron beam-induced deposition (FEBID) as a scaffold for plasmonic materials.[27] The FEBID scaffolds were subsequently coated with SiO_2 and Au. The 22 nm conformal SiO_2 layer was deposited via ALD to enhance the structural integrity of the scaffolds, which also isolates the Au layer from the PtC_x scaffold to minimize possible plasmon damping. Due to its well-known plasmonic properties as well as its stability in the atmosphere, 25 nm Au was subsequently deposited on the scaffolds via dc magnetron sputtering (7 W, 3 mTorr).

https://doi.org/10.1021/acsaom.2c00157
ACS Appl. Opt. Mater. 2023, 1, 607–614

Experimental STEM-EELS Measurements

Low-loss EEL spectra were collected using a Nion aberration-corrected high-energy resolution monochromated EELS-STEM instrument (Nion HERMES) operating at an accelerating voltage of 100 kV. Point spectra and spectrum images were collected with a convergence semiangle of 30 mrad and a collection semiangle of 15 mrad, with a beam current of ∼8 pA.[36,37] Scattered electrons were dispersed in a Nion Iris spectrometer at 1.2 meV/channel, and the energy resolution [full width at half-maximum of the zero loss peak (ZLP)] was approximately 16 meV. Point spectra had their ZLP maxima normalized to unity.

Numerical EELS Simulations

Simulations of the EEL spectra were performed using the electron-driven discrete dipole approximation (*e*-DDA).[38,39] The SRR shapes were modeled as toroids cut according to the geometry and dimensions of the experiment. We note that the non-metal layers, substrates, and pillar were omitted to simplify the simulations. The electron beam energy was set at 100 keV, and the impact parameters for all spectra were recorded between 9 and 12 nm. The tabulated dielectric data for gold in ref 40 were used, and all field maps were calculated 45 nm above the plane containing the SRR structures.

AUTHOR INFORMATION

Corresponding Authors

Philip D. Rack − *Department of Materials Science and Engineering, University of Tennessee, Knoxville, Tennessee 37996, United States; Center for Nanophase Materials Science, Oak Ridge National Laboratory, Oak Ridge, Tennessee 37831, United States;* orcid.org/0000-0002-9964-3254; Email: prack@utk.edu

David J. Masiello − *Department of Chemistry, University of Washington, Seattle, Washington 98195, United States;* orcid.org/0000-0002-1187-0920; Email: masiello@uw.edu

Authors

C. Praise Anyanwu − *Department of Chemistry, University of Washington, Seattle, Washington 98195, United States*

Grace Pakeltis − *Department of Materials Science and Engineering, University of Tennessee, Knoxville, Tennessee 37996, United States;* orcid.org/0000-0003-1478-4654

Complete contact information is available at: https://pubs.acs.org/10.1021/acsaom.2c00157

Author Contributions

‖C.P.A. and G.P. contributed equally to this work.

Notes

The authors declare no competing financial interest.

ACKNOWLEDGMENTS

G.P. and P.D.R. acknowledge support from the National Science Foundation under Grant DMR 1709275. Work at the University of Washington was supported by the U.S. National Science Foundation under Grants CHE-1954393 and QII-TAQS-1936100 (C.P.A. and D.J.M.). All of the authors acknowledge that the nanofabrication and high-energy resolution EELS measurements were conducted at the Center for Nanophase Materials Sciences, which is a U.S. Department of Energy Office (DOE) of Science User Facility. This research was conducted, in part, using instrumentation within Oak Ridge National Laboratory's Materials Characterization Core provided by UT-Battelle, LLC, under Contract DE-AC05-00OR22725 with the DOE and sponsored by the Laboratory Directed Research and Development Program of Oak Ridge National Laboratory, managed by UT-Battelle, LLC, for the DOE.

REFERENCES

(1) Silveirinha, M. G.; Fernandes, C. A. Nonresonant structured material with extreme effective parameters. *Phys. Rev. B* **2008**, *78*, 033108.

(2) Ziolkowski, R. W. Propagation in and scattering from a matched metamaterial having a zero index of refraction. *Phys. Rev. E* **2004**, *70*, 046608.

(3) Pendry, J. B.; Holden, A. J.; Robbins, D. J.; Stewart, W. Magnetism from conductors and enhanced nonlinear phenomena. *IEEE Transactions on Microwave Theory and Techniques* **1999**, *47*, 2075−2084.

(4) Liu, Y.; Zhang, X. Metamaterials: a new frontier of science and technology. *Chem. Soc. Rev.* **2011**, *40*, 2494−2507.

(5) Smith, D. R.; Padilla, W. J.; Vier, D.; Nemat-Nasser, S. C.; Schultz, S. Composite medium with simultaneously negative permeability and permittivity. *Phys. Rev. Lett.* **2000**, *84*, 4184.

(6) Shelby, R. A.; Smith, D. R.; Schultz, S. Experimental verification of a negative index of refraction. *Science* **2001**, *292*, 77−79.

(7) Smith, D. R.; Pendry, J. B.; Wiltshire, M. C. Metamaterials and negative refractive index. *Science* **2004**, *305*, 788−792.

(8) Shalaev, V. M. Optical negative-index metamaterials. *Nat. Photonics* **2007**, *1*, 41−48.

(9) Pendry, J. B. Negative refraction makes a perfect lens. *Phys. Rev. Lett.* **2000**, *85*, 3966.

(10) Pendry, J.; Ramakrishna, S. A. Focusing light using negative refraction. *J. Phys.: Condens. Matter* **2003**, *15*, 6345.

(11) Pendry, J. B.; Schurig, D.; Smith, D. R. Controlling electromagnetic fields. *Science* **2006**, *312*, 1780−1782.

(12) Kadic, M.; Milton, G. W.; van Hecke, M.; Wegener, M. 3D metamaterials. *Nature Reviews Physics* **2019**, *1*, 198−210.

(13) Lee, H.-J.; Lee, J.-H.; Moon, H.-S.; Jang, I.-S.; Choi, J.-S.; Yook, J.-G.; Jung, H.-I. A planar split-ring resonator-based microwave biosensor for label-free detection of biomolecules. *Sens. Actuators, B* **2012**, *169*, 26−31.

(14) Xu, X.; Peng, B.; Li, D.; Zhang, J.; Wong, L. M.; Zhang, Q.; Wang, S.; Xiong, Q. Flexible Visible-Infrared Metamaterials and Their Applications in Highly Sensitive Chemical and Biological Sensing. *Nano Lett.* **2011**, *11*, 3232−3238.

(15) Yu, N.; Aieta, F.; Genevet, P.; Kats, M. A.; Gaburro, Z.; Capasso, F. A Broadband, Background-Free Quarter-Wave Plate Based on Plasmonic Metasurfaces. *Nano Lett.* **2012**, *12*, 6328−6333.

(16) Falcone, F.; Lopetegi, T.; Laso, M. A. G.; Baena, J. D.; Bonache, J.; Beruete, M.; Marqués, R.; Martín, F.; Sorolla, M. Babinet Principle Applied to the Design of Metasurfaces and Metamaterials. *Phys. Rev. Lett.* **2004**, *93*, 197401.

(17) Glybovski, S. B.; Tretyakov, S. A.; Belov, P. A.; Kivshar, Y. S.; Simovski, C. R. Metasurfaces: From microwaves to visible. *Phys. Rep.* **2016**, *634*, 1−72.

(18) Cheng, Y.; Yang, H.; Cheng, Z.; Wu, N. Perfect metamaterial absorber based on a split-ring-cross resonator. *Appl. Phys. A: Mater. Sci. Process.* **2011**, *102*, 99−103.

(19) Liu, N.; Liu, H.; Zhu, S.; Giessen, H. Stereometamaterials. *Nat. Photonics* **2009**, *3*, 157−162.

(20) Powell, D. A.; Lapine, M.; Gorkunov, M. V.; Shadrivov, I. V.; Kivshar, Y. S. Metamaterial tuning by manipulation of near-field interaction. *Phys. Rev. B* **2010**, *82*, 155128.

(21) Liu, N.; Giessen, H. Coupling effects in optical metamaterials. *Angew. Chem., Int. Ed.* **2010**, *49*, 9838−9852.

(22) Liu, N.; Kaiser, S.; Giessen, H. Magnetoinductive and electroinductive coupling in plasmonic metamaterial molecules. *Adv. Mater.* **2008**, *20*, 4521−4525.

(23) von Cube, F.; Irsen, S.; Niegemann, J.; Matyssek, C.; Hergert, W.; Busch, K.; Linden, S. Spatio-spectral characterization of photonic

meta-atoms with electron energy-loss spectroscopy. *Optical Materials Express* **2011**, *1*, 1009−1018.
(24) von Cube, F.; Irsen, S.; Diehl, R.; Niegemann, J.; Busch, K.; Linden, S. From isolated metaatoms to photonic metamaterials: evolution of the plasmonic near-field. *Nano Lett.* **2013**, *13*, 703−708.
(25) Liang, Q.; Wen, Y.; Mu, X.; Reindl, T.; Yu, W.; Talebi, N.; van Aken, P. A. Investigating hybridization schemes of coupled split-ring resonators by electron impacts. *Opt. Express* **2015**, *23*, 20721.
(26) Bicket, I. C.; Bellido, E. P.; Meuret, S.; Polman, A.; Botton, G. A. Correlative electron energy loss spectroscopy and cathodoluminescence spectroscopy on three-dimensional plasmonic split ring resonators. *Microscopy* **2018**, *67*, i40−i51.
(27) Pakeltis, G.; Hu, Z.; Nixon, A. G.; Mutunga, E.; Anyanwu, C. P.; West, C. A.; Idrobo, J. C.; Plank, H.; Masiello, D. J.; Fowlkes, J. D.; Rack, P. D. Focused Electron Beam Induced Deposition Synthesis of 3D Photonic and Magnetic Nanoresonators. *ACS Applied Nano Materials* **2019**, *2*, 8075−8082.
(28) Liu, H.; Genov, D.; Wu, D.; Liu, Y.; Steele, J.; Sun, C.; Zhu, S.; Zhang, X. Magnetic plasmon propagation along a chain of connected subwavelength resonators at infrared frequencies. *Phys. Rev. Lett.* **2006**, *97*, 243902.
(29) Quillin, S. C.; Cherqui, C.; Montoni, N. P.; Li, G.; Camden, J. P.; Masiello, D. J. Imaging Plasmon Hybridization in Metal Nanoparticle Aggregates with Electron Energy-Loss Spectroscopy. *J. Phys. Chem. C* **2016**, *120*, 20852−20859.
(30) Garcia De Abajo, F. J. Optical excitations in electron microscopy. *Rev. Mod. Phys.* **2010**, *82*, 209.
(31) Seetharaman, S.; King, C.; Hooper, I.; Barnes, W. Electromagnetic interactions in a pair of coupled split-ring resonators. *Phys. Rev. B* **2017**, *96*, 085426.
(32) Powell, D. A.; Hannam, K.; Shadrivov, I. V.; Kivshar, Y. S. Near-field interaction of twisted split-ring resonators. *Phys. Rev. B* **2011**, *83*, 235420.
(33) Liu, H.; Genov, D.; Wu, D.; Liu, Y.; Liu, Z.; Sun, C.; Zhu, S.; Zhang, X. Magnetic plasmon hybridization and optical activity at optical frequencies in metallic nanostructures. *Phys. Rev. B* **2007**, *76*, 073101.
(34) Hesmer, F.; Tatartschuk, E.; Zhuromskyy, O.; Radkovskaya, A. A.; Shamonin, M.; Hao, T.; Stevens, C. J.; Faulkner, G.; Edwards, D. J.; Shamonina, E. Coupling mechanisms for split ring resonators: Theory and experiment. *Physica Status Solidi (b)* **2007**, *244*, 1170−1175.
(35) Smith, K. C.; Chen, Y.; Majumdar, A.; Masiello, D. J. Active tuning of hybridized modes in a heterogeneous photonic molecule. *Physical Review Applied* **2020**, *13*, 044041.
(36) Krivanek, O. L.; Lovejoy, T. C.; Dellby, N.; Aoki, T.; Carpenter, R.; Rez, P.; Soignard, E.; Zhu, J.; Batson, P. E.; Lagos, M. J.; Egerton, R. F.; Crozier, P. A. Vibrational spectroscopy in the electron microscope. *Nature* **2014**, *514*, 209−212.
(37) Hachtel, J. A.; Lupini, A. R.; Idrobo, J. C. Exploring the capabilities of monochromated electron energy loss spectroscopy in the infrared regime. *Sci. Rep.* **2018**, *8*, 5637.
(38) Bigelow, N. W.; Vaschillo, A.; Iberi, V.; Camden, J. P.; Masiello, D. J. Characterization of the electron-and photon-driven plasmonic excitations of metal nanorods. *ACS Nano* **2012**, *6*, 7497−7504.
(39) Bigelow, N. W.; Vaschillo, A.; Camden, J. P.; Masiello, D. J. Signatures of Fano interferences in the electron energy loss spectroscopy and cathodoluminescence of symmetry-broken nanorod dimers. *ACS Nano* **2013**, *7*, 4511−4519.
(40) Olmon, R. L.; Slovick, B.; Johnson, T. W.; Shelton, D.; Oh, S.-H.; Boreman, G. D.; Raschke, M. B. Optical dielectric function of gold. *Phys. Rev. B* **2012**, *86*, 235147.

https://doi.org/10.1021/acsaom.2c00157
ACS Appl. Opt. Mater. 2023, 1, 607−614